

The Observed Influence of Tropical Convection on the Saharan Dust Layer

Kathryn Sauter¹ , Tristan S. L'Ecuyer^{1,3}, Susan C. van den Heever² , Cynthia Twohy³ , Andrew Heidinger⁴, Steve Wanzong⁴, and Norm Wood⁵ 

¹Department of Atmospheric and Oceanic Sciences, University of Wisconsin-Madison, Madison, WI, USA, ²Department of Atmospheric Science, Colorado State University, Fort Collins, CO, USA, ³NorthWest Research Associates, Inc., Redmond, WA, USA, ⁴Cooperative Institute for Meteorological Satellite Studies, University of Wisconsin-Madison, Madison, WI, USA, ⁵Space Science and Engineering Center, University of Wisconsin-Madison, Madison, WI, USA

Key Points:

- Active and passive satellite observations document the influence of tropical storm systems on dust transport over the Atlantic Ocean
- Convection accounts for $15\% \pm 7\%$ of dust deposition in the Atlantic where 85% is removed by dry deposition or from nonconvective events
- Tropical convection lofts $1.5\% \pm 0.6\%$ of dust mass from the Saharan Air Layer to altitudes greater than 6 km

Supporting Information:

- Supporting Information S1

Correspondence to:

K. Sauter,
sauter2@wisc.edu

Citation:

Sauter, K., L'Ecuyer, T. S., van den Heever, S. C., Twohy, C., Heidinger, A., & Wood, N. (2019). The observed influence of tropical convection on the Saharan dust layer. *Journal of Geophysical Research: Atmospheres*, 124, 10,896–10,912. <https://doi.org/10.1029/2019JD031365>

Received 17 JUL 2019

Accepted 11 SEP 2019

Accepted article online 15 OCT 2019

Published online 31 OCT 2019

Abstract Interactions between convection and the Saharan Air Layer in the tropical Atlantic Ocean are quantified using a novel compositing technique that leverages geostationary cloud observations to add temporal context to the polar orbiting CloudSat and the Cloud Aerosol Lidar and Infrared Pathfinder Satellite Observations (CALIPSO) satellites allowing aerosol optical depth (AOD) changes to be tracked throughout a typical convective storm life cycle. Four years of CALIPSO observations suggests that approximately 20% of the dust mass in every 10° longitude band between 10°W and 80°W is deposited into the ocean. Combining a new convective identification algorithm based on hourly geostationary cloud products with AOD_{dust} profiles along the CALIPSO track reveals that wet scavenging by convection is responsible for a significant fraction of this deposition across the Atlantic. Composites of 4 years of convective systems reveal that, on average, convection accounts for $15\% \pm 7\%$ of the dust deposition in each longitude band relative to preconvective amounts, implying that dry deposition and scavenging by nonconvective events are responsible for the remaining 85% of dust removal. In addition, dust layers are detrained at upper levels of the atmosphere between 8 and 12 km by convective storms across the Atlantic. The dust budget analysis presented here indicates that convection lofts $1.5\% \pm 0.6\%$ of dust aerosol mass to altitudes greater than 6 km. This may have significant implications for cloud formation downstream of convection since lofted dust particles can act as effective ice nucleating particles, altering cloud microphysical and radiative properties, latent heating, and precipitation rates.

1. Introduction

Dust aerosols are recognized to affect Earth's climate in a variety of significant ways such as influencing the global radiation budget, altering the cloud microphysics and precipitation, creating an aerosol indirect effect on cloud properties, and generating a longwave direct radiative effect (Brindley & Russell, 2009; Min et al., 2009; Sassen et al., 2003; Tegen et al., 1996). Globally, dust aerosols constitute the highest atmospheric mass loading of atmospheric aerosols besides sea salt, especially downwind of Africa and other desert regions (Tegen & Fung, 1995). Compared to other atmospheric aerosols, dust covers the largest area and occurs most frequently in the atmosphere (Husar et al., 1997). Small dust particles can be transported both horizontally and vertically and have the ability to modify cloud frequency, properties, and lifetimes by acting as cloud condensation nuclei and Ice Nucleating Particle (Storer et al., 2014; Van den Heever et al., 2006). In addition, dust impacts the radiation budget through scattering and absorption, with a predicted negative net radiative forcing globally through direct and indirect effects (Mahowald et al., 2010; Myhre et al., 2003; Tegen et al., 1996). Marine biogeochemical processes are also affected by mineral dust through the increased nutrients in oceanic regions, as dust is a large source of iron and other micronutrients (Duce, 1986; Fung et al., 2000; Zhu et al., 1997).

However, while dust aerosols have been studied extensively, there are still large uncertainties in predicting the processes that affect the total amount of dust in the atmosphere, particularly that impact amount that originates from the Saharan Desert. Kaufman et al. (2005) used observations from the Moderate Resolution Imaging Spectrometer to estimate that 240 ± 80 Tg of dust is transported annually from Africa to the Atlantic Ocean, while the Cloud Aerosol Lidar and Infrared Pathfinder Satellite Observations (CALIPSO) observations suggest that only 24% of dust that leaves the African coast reaches 75°W (Yu et al., 2015). The majority

of this dust resides in the Saharan Air Layer (SAL), which is a thermodynamically stable mixture of elevated warm and dry air that extends up to 7,000 km across the tropical Atlantic Ocean (Carlson & Prospero, 1972; Dunion & Velden, 2004).

Several studies have investigated the impact of dust in the SAL on clouds, particularly large convective storm systems that originate from African Easterly Waves (Braun, 2010; Dunion & Velden, 2004; Herbener et al., 2014, 2016; Karyampudi & Pierce, 2002; Pratt & Evans, 2009; Rosenfeld et al., 2011). The effect of convection on the dust layer is, however, much less studied. Evan et al. (2006) suggested that the SAL acts as a control on tropical Atlantic cyclone activity. The SAL is found to suppress tropical cyclone activity in the Atlantic Ocean by introducing dry, stable air into the storm, leading to convectively driven downdrafts in the tropical cyclone. The enhancement of local vertical wind shear from the SAL's midlevel easterly jet and the preexisting trade wind inversion in the Atlantic stabilizes the environment and suppresses tropical cyclone activity. Tropical storms can also be enhanced after emerging from the SAL and develop into strong hurricanes (Dunion & Velden, 2004). The presence of dust has also been found to impact the intensity of hurricanes through aerosol impacts on the microphysics, cold pools, and latent heating (Herbener et al., 2014; Rosenfeld et al., 2011). These, and other related studies, also provide evidence that tropical cyclones induce reciprocal changes in the dust loadings within the SAL. This effect was quantified through satellite observations of three tropical storms in Sauter and L'Ecuyer (2017), hereafter SL17, where it was found that individual tropical cyclones may scavenge up to two thirds of the dust in the SAL.

The goal of this research is to generalize the findings of SL17 to quantify the net influence overall implications on convective activity in the tropical Atlantic Ocean for the transport of Saharan dust. Our main objectives are to determine both the fraction of dust that is removed from the atmosphere through wet deposition processes and the fraction that is transported to the upper troposphere by tropical convective storm systems. The analysis includes both isolated convection and mesoscale convective systems, which are the dominant systems for transporting water vapor and energy vertically into the atmosphere (Tobin et al., 2012). These systems include both large individual cells contributing to squall lines or mesoscale complexes, as well as those that group together to form larger superclusters (Houze, 2004; Mapes & Houze, 1993). As a result, mesoscale convective systems have a variety of cloud and precipitation structures that include areas of convective and stratiform clouds and precipitation. Such systems develop mesoscale circulations as they mature that may also transport dust vertically through the atmosphere (Houze, 2014).

To capture the full vertical profile of dust aerosols through a typical convective life cycle, aerosol observations from the Cloud Aerosol Lidar and Infrared Pathfinder Satellite Observations (CALIPSO) satellite are composited with respect to convection identified within the Pathfinder Atmospheres Extended (PATMOS-x) cloud product data set (Heidinger et al., 2012; Winker et al., 2003). CALIPSO has the ability to provide highly resolved vertical profiles of dust aerosols that have been lacking from other instruments (Liu et al., 2008). PATMOS-x adds a new time component to the CALIPSO observations allowing their statistical evolution across the convective life cycle to be stitched together based on thousands of independent overpasses.

2. Data Sets

2.1. CloudSat and CALIPSO

Launched in 2006, Cloudsat and CALIPSO are a part of the afternoon Train (A-Train) satellite constellation (L'Ecuyer & Jiang, 2010). These satellites fly in Sun-synchronous, polar orbits at an altitude of 705 km, and an inclination of 98° with equatorial crossing times at approximately 01:30 and 13:30 local time and a 16-day repeat cycle (Stephens et al., 2002; Yu et al., 2010). CloudSat carries a nadir-viewing, high-power, W-band pulsed radar termed the Cloud Profiling Radar, which is the first-ever millimeter wave radar launched into space and measures the power backscatter from clouds and precipitation. The instrument operates at 94.05 gigahertz (GHz) with −30-decibel (dBz) sensitivity making it ideally suited for identifying the extent of cirrus anvils and distinguishing the stratiform and convective regions of storms (Deng et al., 2010; Haynes et al., 2009; Igel et al., 2014; Im et al., 2005; Lebsock et al., 2011).

CALIPSO provides high-resolution vertical profiles of aerosols and clouds from backscatter measurements obtained by its Cloud-Aerosol Lidar with Orthogonal Polarization (CALIOP; Winker et al., 2003). CALIOP acquires vertical profiles (of two orthogonal polarization components) of attenuated backscatter by clouds and aerosols at a visible wavelength of 532 nm and a total backscatter laser signal at an infrared wavelength of 1,064 nm (Liu et al., 2012). Spherical liquid droplets and larger ice particles and dust are distinguished

through the combination of 532-nm backscatter, depolarization ratio, and ratio of backscatter at 1,064 to 532 nm. CALIOP level 1b source data have a physical separation of 335 m between each footprint and are collocated with the CloudSat radar footprint based on the same resolution and location, allowing for the powerful three-dimensional structure of clouds and aerosol (Liu et al., 2012).

Here, the collocated CALIPSO data from Version 3 CALIOP L2 cloud layer data and aerosol layer data on a 5-km horizontal grid (CAL_LID_L2_05kmCLay and CAL_LID_L2_05kmALay) products are used to define the AOD and aerosol type of each scene. While Version 4 CALIPSO Level 2 data are now available for processing, careful examination of case studies by SL17 revealed that the change from Version 3 to Version 4 does not significantly change the results of the composite analyses presented below. Aerosols are classified into six types (marine, polluted continental, clean continental, dust, polluted dust, and smoke) using a cluster analysis from AERONET measurements as described in Omar et al. (2009). The CALIPSO dust model is based on theoretical particle scattering by using the discrete-dipole approximation technique, while the polluted dust model is designed to account for dust particles mixed with biomass burning smoke (Omar et al., 2009). In this study, both dust and polluted dust aerosols are added together when calculating AOD and will be represented as AOD_{dust} . AOD_{dust} is defined as the column-integrated dust extinction.

Uncertainties in the CALIPSO aerosol observations employed here stem from several sources. Misclassification of the aerosol type contributes to uncertainty in dust extinction estimates due to ambiguity with the determination of the extinction to backscatter or lidar ratio. The fractional uncertainty of smaller AODs can be approximated as the fractional uncertainty of the lidar ratio, typically about 30% on the large averaging scales characteristic of this work. AODs between 0.01 and 0.6 correspond to 30% errors in selecting lidar ratios between 0.2 and 0.6. Larger AODs, greater than 0.6, have higher uncertainties as the fractional uncertainty of the lidar ratio increases (Winker et al., 2009). An additional uncertainty arises when the lidar signal is either fully attenuated in layers with high AODs or when the detection algorithm incorrectly identifies clear air while still inside the aerosol layer, leading to a misclassification of the aerosol layer base (Yu et al., 2010). CALIPSO may also miss extremely thin layers and may classify heavy dust or smoke layers as clouds (Winker et al., 2009). The Cloud-Aerosol Discrimination (CAD) score can be used in order to determine the confidence in detecting a cloud. CAD scores indicate the confidence level of feature classifications such as clouds and aerosols, with higher magnitudes representing a higher certainty. While we did not explicitly screen scenes using CAD scores, visual inspection suggests that they were typically high for the scenes considered here. In addition, low CAD scores are typically associated with low-level cloud occurrences (<1 km), where this study focuses on upper levels in the atmosphere (Ham et al., 2017). A comprehensive analysis of the CALIOP aerosol detection and algorithm is located in several publications (Liu et al., 2009; Omar et al., 2009; Winker et al., 2009; Young et al., 2013).

As thick clouds are likely to influence CALIPSO dust signals, collocated reflectivities from the CloudSat Cloud Profiling Radar are used to identify precipitation and convection and screen cloudy pixels in the analysis (Henderson et al., 2013; Liu et al., 2012). The convective flag from Cloudsat's 2C-Column-Integrated Precipitation Retrieval Product is used to identify convective profiles in each 5textdegree longitude band across the tropical Atlantic. Liquid precipitation causes significant attenuation of the W-Band reflectivity profile and, therefore, provides a very precise method for delineating precipitation (Haynes et al., 2009). Each rain-certain pixel is further identified as either stratiform, convective, or shallow based on the vertical structure of reflectivity. Since liquid precipitation causes significant attenuation of the W-band radar reflectivity profile, the strong updrafts characteristic of convective cores exhibit a sharp decrease in reflectivity at high altitudes due to the liquid water lofted above the 0 °C freezing level. This is distinct from stratiform precipitation that is characterized by primarily ice phase above the freezing level, a well-defined melting layer approximately 500 m below the freezing level, and liquid precipitation below that. As a result, convective profiles can be delineated very precisely by identifying those where attenuation is evident above the freezing level in the reflectivity profiles (Bouniol et al., 2016; Haynes et al., 2014).

2.2. PATMOS-x

PATMOS-x is a satellite-based climate data record generated by the National Oceanic and Atmospheric Administration and more recently the European Organisation for the Exploitation of Meteorological Satellites Meteorological Operational satellite programme satellites (Heidinger et al., 2012; Schmetz et al., 2002). The PATMOS-x data set supplies cloud and aerosol information from calibrated Advanced Very High Resolution Radiometer (AVHRR) observations and selected ancillary data that have been made from various

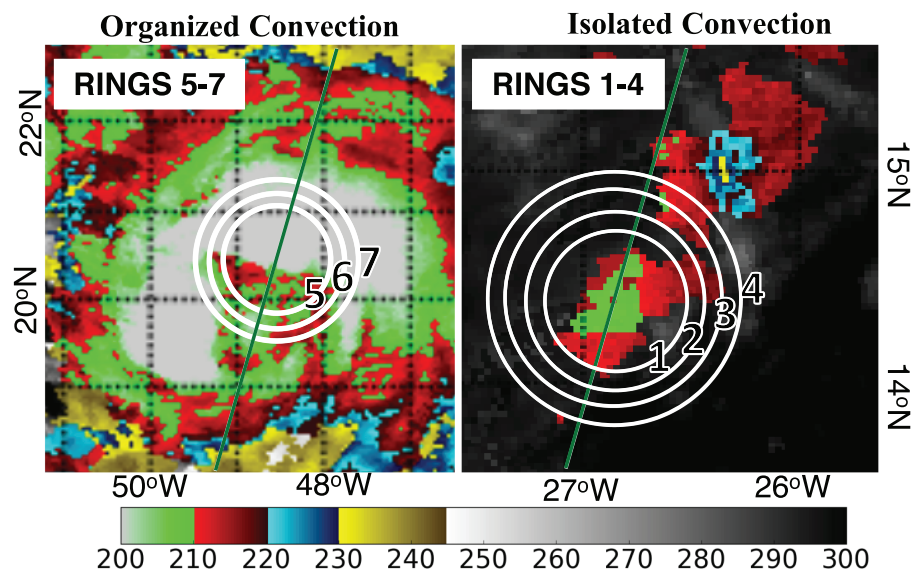
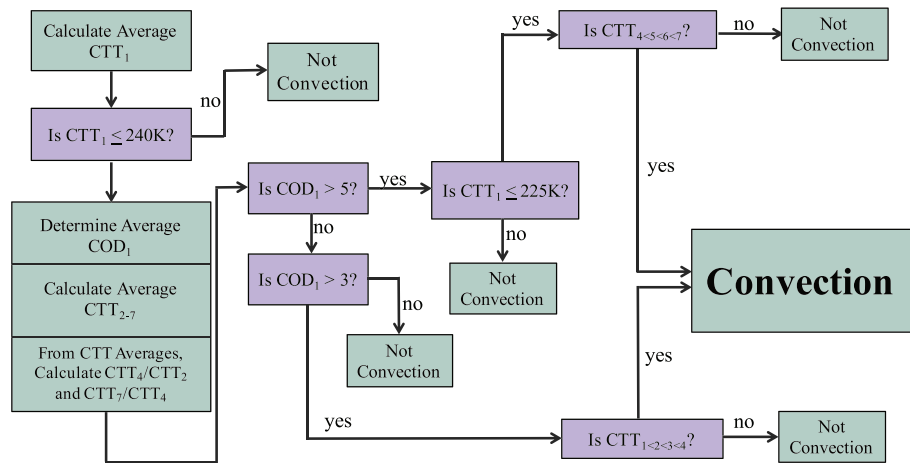


Figure 1. Flow chart depicting the procedure for identifying organized and isolated convection using the Pathfinder Atmospheres Extended data. The subscripts, *i*, on CTT_i and COD_i correspond to the areal footprint sizes and areas summarized in Table 1. Conceptual illustration of organized and isolated convective systems is shown at the bottom with the areal rings used to determine the CTTs and CODs used in the algorithm. Note: The rings are not drawn to scale. The corresponding the Cloud Aerosol Lidar and Infrared Pathfinder Satellite Observations overpass is shown in green for reference. CTT = cloud top temperature; COD = cloud optical depth.

the National Oceanic and Atmospheric Administration satellite instruments since 1978. AVHRR visible and infrared radiances provide information for detecting clouds on a global scale at a spatial resolution of 1.1 km at nadir over the full Geostationary Operational Environmental Satellite (GOES) swath (Heidinger et al., 2014; Sun et al., 2015). Meteosat satellites are equipped with the Spinning Enhanced Infrared Imager for continuous observation of the Earth. The Spinning Enhanced Infrared Imager consists of 12 visible and infrared channels to detect cloud properties. Cloud properties and products are also generated from Meteosat using the AVHRR PATMOS-x algorithms, similar to GOES East. (Schmetz et al., 2002). PATMOS-x employs a level-1b file format that is composed of sampled pixels, allowing for the conversion of observations of brightness temperatures into radiances. Clouds are detected using a naive Bayesian cloud mask algorithm that is collocated with the polar-orbiting CALIPSO data to create a $0.1^\circ \times 0.1^\circ$ PATMOS-x product (Heidinger et al., 2012). A full description of the algorithm is located in recent publications (Pavolonis et al., 2005; Walther & Heidinger, 2012).

Table 1 Dimensions of Each Areal Footprint Used in the Convective Identification Algorithm

Footprint size (FS)	Diameter (pixels)	Radius (km)	Area (km ²)
1	3	18	1053
2	5	29	2,561
3	7	40	4,901
4	9	50	7,969
5	11	68	14,677
6	13	79	19,721
7	15	94	27,573

PATMOS-x cloud products from the GOES East and Meteosat Second Generation data sets are used to place the cloud and aerosol snapshots from CloudSat and CALIPSO into the context of the evolution and intensity of convection. Data from the two separate geostationary satellites cover the full extent of the tropical Atlantic Ocean in our region of interest from 0–35°N to 10–80°W. GOES East spans the region from 40°W to 80°W, while the Meteosat satellites extend coverage to the West Coast of Africa.

2.3. Identifying Convection

To gain insights into the time evolution of the aerosol field in response to the passage of convection, the A-Train data were collocated with time-resolved cloud information from PATMOS-x. This coupling to geostationary observations allows the continuous tracking of convection necessary to associate changes in the vertical structure of dust aerosol distribution to the presence

of convection. PATMOS-x cloud products from the closest sampling time to the A-Train overpass were matched to each pixel along the CloudSat and CALIPSO track using a nearest neighbor approach to acquire cloud properties in the vicinity of the aerosol layer across the entire tropical Atlantic Ocean (10–80°W, 0–35°N). Cloud products were then added from additional observation times before and after the CloudSat and CALIPSO overpass to characterize the time evolution of the cloud field around the overpass. Cloud top temperature (CTT) and cloud optical depth (COD) from the PATMOS-x data were averaged over a range of areal “footprints” centered on the collocated latitude and longitude along the actual CloudSat and CALIPSO ground track for all geostationary observation times between 12 hr prior to and 12 hr after the A-Train observation time.

Convective systems can be identified in PATMOS-x observations based on their areal extent as well as their CTT and COD (Houze, 2004; Liu et al., 1995; Mapes & Houze, 1993; Yuan et al., 2011). We adopt a two-step approach that first utilizes both CTT and COD thresholds. The second step examines the change in CTT with increasing area around each center pixel to identify both isolated and organized convection. The method is illustrated in Figure 1.

For each collocated PATMOS-x pixel, the average CTT is computed for a range of progressively larger areal footprints with diameters from 36 to 188 km (3 to 15 GOES East and Meteosat PATMOS-x pixels). Whenever cloud fraction in a given pixel was less than 0.1, cloud temperatures were replaced with PATMOS-x surface temperatures. In what follows, the subscripts, *i*, on CTT_i and COD_i correspond to the areal footprint sizes and areas summarized in Table 1. Every pixel along the CALIPSO track at all PATMOS-x observation times is simply classified as either convective or not, with the latter including both clear-sky and nonconvective clouds. The flowchart in Figure 1 summarizes the framework. First, cold clouds are screened by requiring that CTT_1 is less than 240 K. If not, the pixel is immediately rendered as having no convection.

Two passes are then made through all cloudy pixels that meet this initial CTT criterion. The first pass screens for possible organized convection in cases where the first ring around the CloudSat/CALIPSO track is filled with optically thick clouds. Large mean optical thickness in the 1,000-km² Ring 1, taken here to mean $COD_1 > 5$, is indicative of spatially extensive thick cloud cover that may be associated with mature convective systems consisting of larger cores and surrounding thick anvil. Conversely, the second pass screens for lower optical depths, which are indicative of either thin cirrus or isolated convective cores surrounded by cloud free areas. To verify the presence of convection in these lower COD pixels, two additional requirements are imposed: (a) The mean CTT in this ring, CTT_1 , must be colder than 225 K, and (b) the average CTT in the larger areal footprints (4 through 7) increases with ring size, characteristic of a single-organized system as opposed to a distribution of smaller systems that will be identified below. Satisfying these two conditions confirms that the lower COD is characteristic of a single-organized system as opposed to a distribution of smaller systems. In practice, CTT increases rapidly beyond the edges of an organized convective system providing a robust measure of the size of the system but such information is not required for the analysis that follows since the fundamental objective is to simply identify where convection occurs.

All pixels that do not satisfy these criteria are then rescreened to identify additional isolated convection that may be missed by the criteria outlined above. Isolated convection may exhibit lower mean optical depths and CTTs in Ring 1 but still requires cold topped clouds. Furthermore, unlike large-scale cirrus, CTT can be expected to rise more quickly with increasing area around isolated convection. Thus, isolated convection is

identified by requiring $COD_1 > 3$ and $CTT_1 < 240$ K, consistent with Arkin and Meisner (1987) and Arkin (1979). To further distinguish isolated convection from large-scale thin cirrus, we further require that mean CTT increase between each of the four smallest rings ($CTT_1 > CTT_2 > CTT_3 > CTT_4$).

It is important to note that this convection identification algorithm is designed to simply give a reasonably robust indication of the presence of convection to provide context for the statistical composites of many CALIPSO overpasses below; it is not designed to provide a robust discrimination of isolated and organized convection, and the distinct regimes presented in Figure 1 are for illustrative purposes only. Several other temperature thresholds have been used for identifying convection in other studies: 215, 219, and 235 K (Arkin, 1979; Arkin & Meisner, 1987; Fu et al., 1990; Maddox, 1980). The thresholds adopted in this study leverage the results of these previous studies to optimize detection of all forms of convection throughout the tropical Atlantic throughout the year, but the analyses that follow are not sensitive to the specific thresholds used. Furthermore, we do not distinguish between organized and isolated convection below since separating the effects of these systems is much more sensitive to how they are defined. The two-step screening process is adopted solely to maximize the probability of detecting all convection by searching for the distinct signatures of both large and small cloud systems separately.

3. Climatological Characteristics of the SAL

3.1. Dust Budget

Before addressing the role of convection explicitly, the amount of dust originating from the Saharan desert and sweeping across the tropical Atlantic Ocean can be quantified using the CALIPSO AOD_{dust} product. Following Kaufman et al. (2005), CALIPSO dust and polluted dust AODs are converted to mass using relationships derived from dust size distributions obtained from several field experiments, AERONET measurements, and model data. The mass column concentration for Saharan dust can be estimated as follows:

$$\frac{M}{AOD_{\text{dust}}} = 2.7 \pm 0.4 \text{ g/m}^{-2} \quad (1)$$

where M represents the average mass concentration of dust in the column. This relation was used by Koren et al. (2006) to calculate the amount of dust transported over large distances, as well as by Haywood et al. (2003) to show physical and optical properties of Saharan dust during the Saharan Dust Experiment. The ability to precisely measure that amount of dust exiting the African continent has proven to be difficult and provides a great deal of uncertainty as there are large differences between several models regarding processes such as emissions, transport, and deposition (Huneeus et al., 2011). As discussed in SL17, as dust size decreases from the African coast to the Caribbean, $\frac{M}{AOD_{\text{dust}}}$ is reduced due to gravitational settling (Maring et al., 2003). However, Kaufman et al. (2005) show that the reduction is small (about 15%), which is less than the error bars in equation (1). Therefore, this effect is not explicitly included in these calculations. As Kaufman et al. (2005) does not distinguish between dust and polluted dust aerosols, the uncertainty caused by combining the two is likely within the error bars. Ryder et al. (2013) show that a significant fraction, 60% to 90%, of giant dust particles (30–200 μm) are deposited within 12 hr of leaving the African continent, although they also found that large dust particles have the ability to travel further in giant dust events. In addition, several studies have shown that larger particles travel further across the ocean than expected (Dulac et al., 1992; Goudie & Middleton, 2001; Weinzierl et al., 2009) and that changes to dust aerosol volume sizes are shown to decrease by only 20% after 10 days of transport, suggesting that significant changes in $\frac{M}{AOD_{\text{dust}}}$ are unlikely in less than 24 hr (Maring et al., 2003).

SL17 applied a similar approach to quantify the impacts of three tropical storms on dust in the SAL. Here, we extend this analysis to the mean AOD_{dust} in each 5° longitude band from 15°W to 80°W using all CALIPSO observations from 2007 to 2010. The resulting dust budget across the tropical Atlantic Ocean is shown in Figure 2. On average, 160 ± 24 Tg of dust is observed between 15°W and 20°W immediately west of the Saharan Desert. As distance increases from the source region, the total dust mass decreases almost linearly to 44 ± 7 Tg at 80°W . This implies that the combination of wet and dry deposition processes removes 1.83 Tg of dust per 100 km. This value is fairly stable throughout all 4 years, ranging from a minimum of 1.52 Tg per 100 km in 2009 to 2.05 Tg per 100 km in 2010. This agrees with the analysis from Yu et al. (2015) using CALIPSO data from 2007 to 2013, who reported 183 Tg of dust leaving the African coast with 43 Tg or 24% reaching 75°W . Our analysis is also consistent with results from Kaufman et al. (2005), who found 240 ± 80 Tg

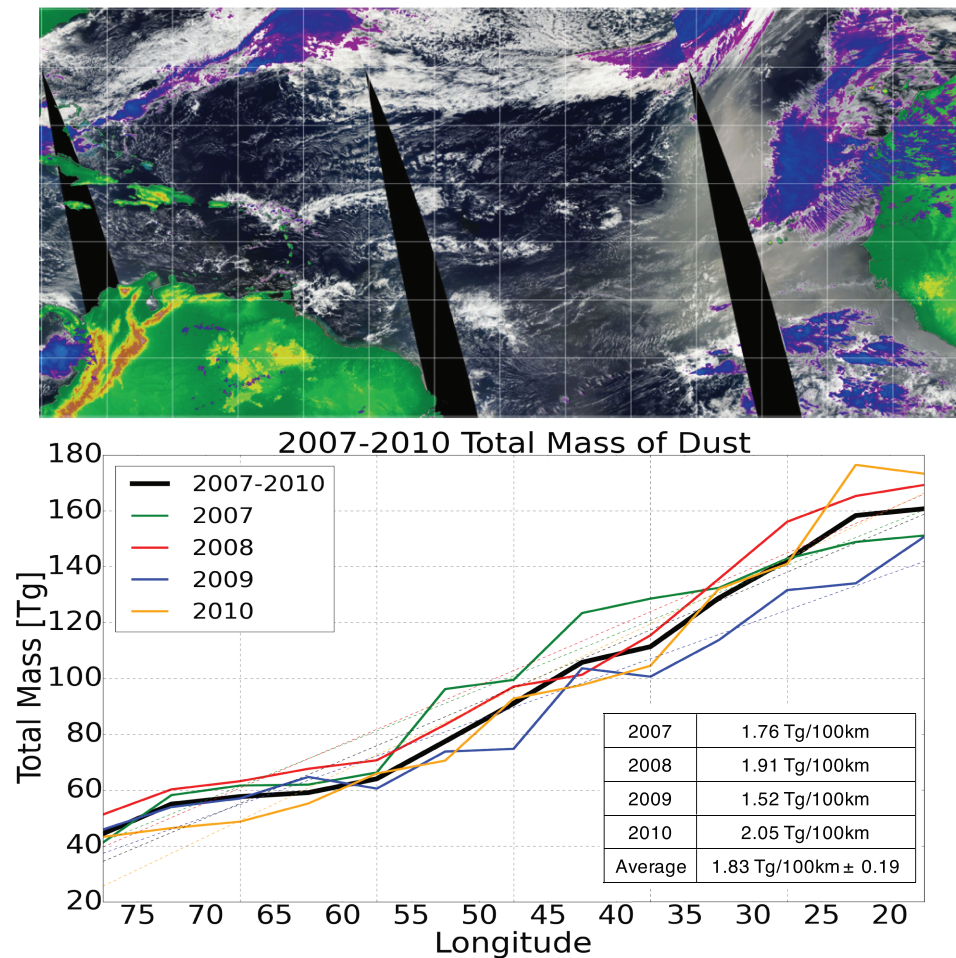


Figure 2. (top) True color example of Saharan dust interacting with convection in the Atlantic basin analyzed in this study (image obtained from the National Aeronautics and Space Administration WorldView). (bottom) Total dust mass (in teragrams) as a function of longitude across the tropical Atlantic Ocean derived from the Cloud Aerosol Lidar and Infrared Pathfinder Satellite Observations between 2007 and 2010. Each band includes the region from 0°N to 35°N. Data have been gridded into 5° longitude bands.

of dust leaving Africa between 20°S and 30°N and 140 ± 40 Tg of dust deposited into the Atlantic Ocean using data from the Moderate Resolution Imaging Spectrometer.

The amount of dust that is deposited into the ocean in each longitude band can be calculated from the estimates in Figure 2 if it is assumed that the latitude bounds between 0°N and 35°N encompass the entire SAL. Although dust from the SAL does extend poleward beyond the 0–35°N domain, there is not a significant amount (approximately 5% of the global dust budget) and would not alter our results (Bullard et al., 2016). During the most active dust season, JJA, Liu et al. (2012) show less than 20% of dust residing between 2 and 4 km beyond 35°N. Less active dust seasons and higher altitudes show less than 10% of total dust amounts beyond 35°N. Since the source of dust is the Sahara Desert and dust is advected westward by the synoptic-scale easterly winds over long time periods, the difference between the mass of dust that enters the eastern edge of a longitude box and exits the western edge must be deposited into the ocean. Although not very common, there are certain meteorological conditions such as significant changes in large-scale subtropical flow or intense depressions that can circulate dust beyond these latitudinal limits and instead transport dust eastward over the Mediterranean sea or north to Northern Europe (Moulin et al., 1998; Reiff et al., 1986). These conditions may contribute to a source of error in the dry deposition estimate.

Figure 3 shows the fractional deposition of dust in each 5° longitude slice across the Atlantic Ocean from 15°W to 80°W for 2007–2010. The graph indicates a relatively constant fraction of about $20\% \pm 12\%$ of dust

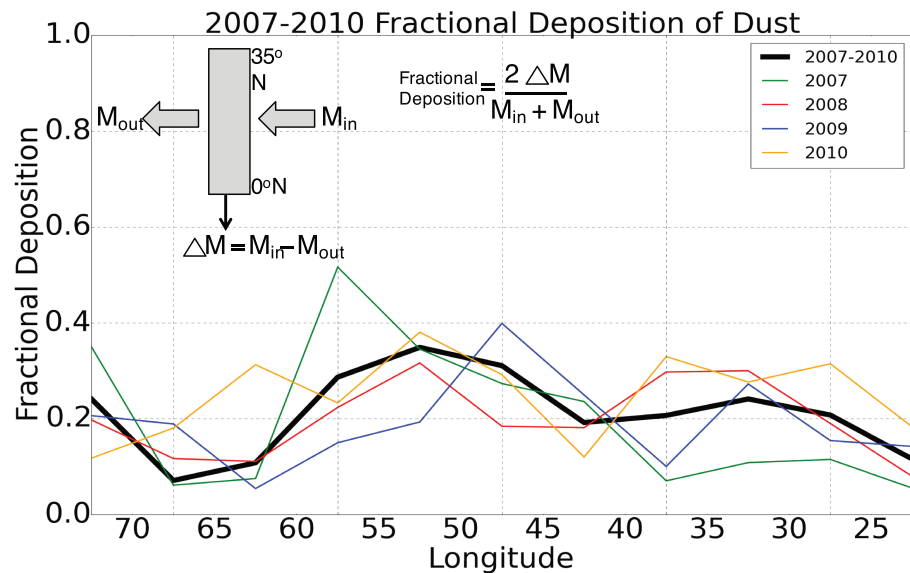


Figure 3. Fractional deposition of dust between 10° longitude bands for 2007–2010. The fractional deposition is the ratio of the mass of dust that is deposited in each longitude band to the total dust mass entering that longitude band. All the Cloud Aerosol Lidar and Infrared Pathfinder Satellite Observations data between 0°N to 35°N are included in these estimates.

deposited in any given longitude band across the tropical Atlantic Ocean. Variations on these multiyear time scales may be due to CALIPSO sampling deficiencies, perhaps owing to clouds.

In addition to the systematic decrease in column-integrated dust amount across the Atlantic, CALIPSO observations also reveal systematic trends in the vertical distribution of dust layers as they propagate westward from the African coast. Figure 4 shows the frequency of dust layers as a function of height for all 13 longitude cross sections across the domain for 2007–2010. The longitude band closest to the African coast, 15–20°W, has the highest frequencies of dust layers within the SAL as it is closest to the dust source, while the longitude band furthest west, 75–80°W, has the lowest frequencies. The SAL is easily distinguishable extending from the surface to approximately 4 km above ground level, near the coast, with the amount of dust in the SAL diminishing almost linearly to approximately 2 km in the westernmost longitude bands. While somewhat harder to see without the enhancement provided in Figure 4, there is a secondary peak in dust layer frequency between 8 and 12 km. While these layers are observed by CALIPSO less than 1% of the time, it is interesting that the maximum frequency of upper level dust layers is not nearest the Sahara Desert but rather located in the longitude band furthest from the coast in the 75–80°W cross section. In the 4-year period examined, CALIOP only detected 641 dust layers above 12 km (from 11,314 total overpasses) and 30% occurred east of 40°W. Conversely, 5,459 dust layers were observed between 8 and 12 km with 954 of those layers as far west as 80°W. CALIOP’s lack of sensitivity to thin layers undoubtedly influences these statistics, but this sensitivity is uniform across the Atlantic so the contrast between lower levels and lofted layers is robust. It is not completely out of the question that a separate dust layer from the SAL is contributing to these elevated layers. Large dust events during the spring in China and Mongolia have the ability to travel across the Pacific Ocean and to North America, therefore potentially contributing to low frequencies of upper level dust in the western Atlantic Ocean (Grousset et al., 2003). Since the majority of the dust in this region is located in the SAL that resides much lower than 8 km, one might conjecture that convection may be responsible for transporting dust to these altitudes.

3.2. Precipitation and Convective Influence on Dust

Adding further support for this inference, convective rainfall fraction from the CloudSat precipitation 2C-Column-Integrated Precipitation Retrieval Product data set is compared against the fraction of elevated dust layers in two, 2-km thick height bins from 6–8 to 8–10 km and greater than 10 km in Figure 5. The elevated dust layer fractions for each height bin follow the same trend as the convective fraction; both increase from east to west across the tropical Atlantic Ocean. In fact, applying a simple linear regression indicates

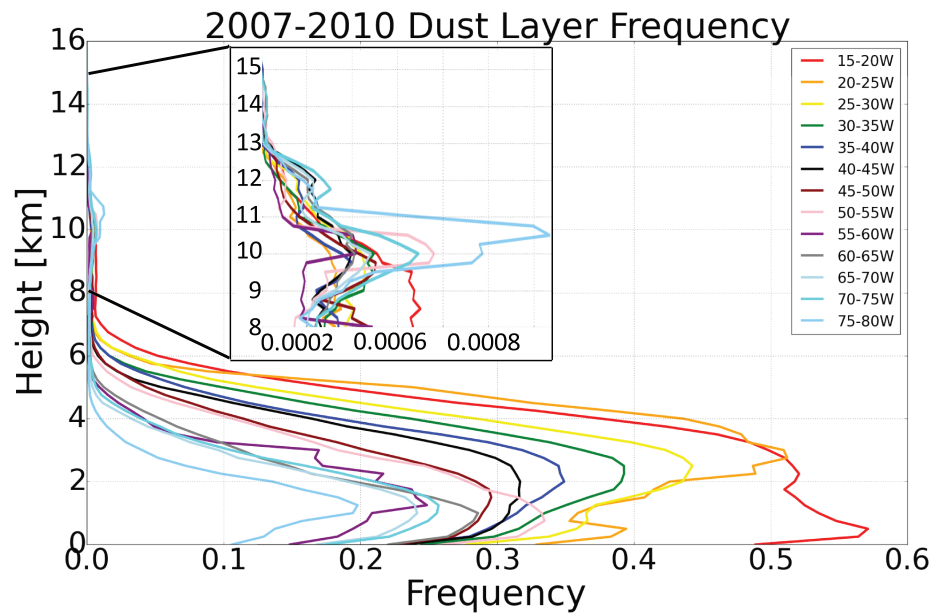


Figure 4. Observed frequency of dust layers for all 5° longitude bands between 0°N and 35°N.

that the correlation between the number of elevated layers between 6 and 12 km and convective rainfall fraction is 0.77. While this simple correlation does not demonstrate causality, it suggests that there may be a link between elevated dust layers and convection in these two independent data sets. Previous modeling studies (Herbener et al., 2016; Prospero, 1996) and individual observational case studies have provided strong evidence that large, convective, storm systems can exert a significant local influence on the redistribution of SAL dust to upper levels of the atmosphere (Chen et al., 2011; Zipser et al., 2009; SL17), but this may be the first direct observational evidence linking elevated dust layer frequency to convective frequency across the tropical Atlantic. Thus, the time evolution of the dust layer as convection passes must be explicitly examined. Since it is not possible to ascribe temporal evolution to individual CALIPSO snapshots, we adopt a novel compositing procedure analogous to that first described in Masunaga (2012).

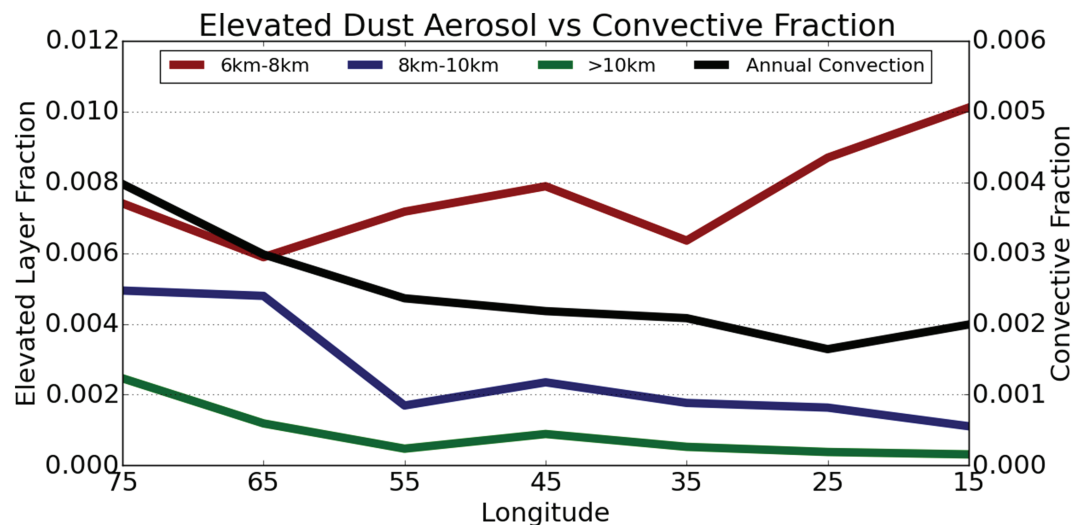
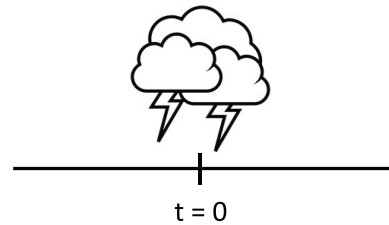
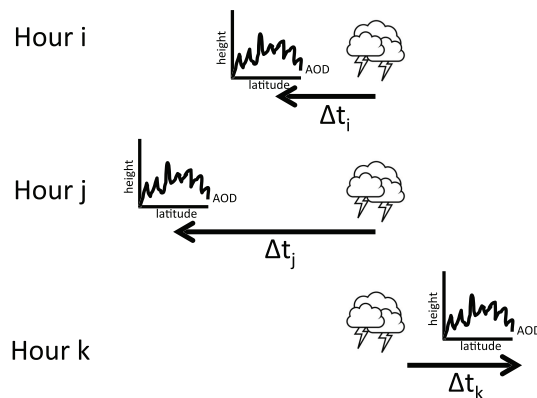


Figure 5. Comparison of the Cloud Aerosol Lidar and Infrared Pathfinder Satellite Observations elevated dust layer fractions and CloudSat annual convective area fraction across the Tropical Atlantic.

1. Identify Convection



2. Individual A-Train Observations



3. Composite Time

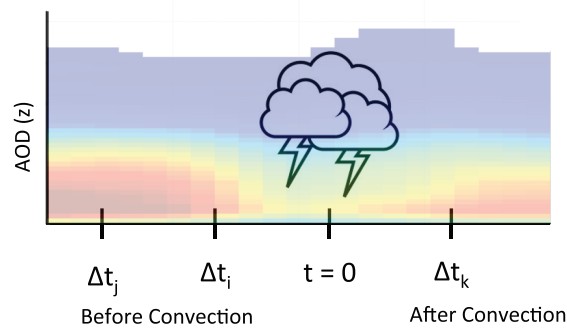


Figure 6. Schematic adapted from Masunaga (2012) outlining the composite analysis. The first step is to identify convection using the Pathfinder Atmospheres Extended convective algorithm. The Cloud Aerosol Lidar and Infrared Pathfinder Satellite Observations aerosol optical depth observations on the same day at the same location are then identified. The Cloud Aerosol Lidar and Infrared Pathfinder Satellite Observations observations are then composited according to their time difference relative to the identified storm.

4. Composite Evolution of the Dust Layer

To better understand the role convection plays in determining the dust budget and vertical structure of Saharan dust as it crosses the tropical Atlantic, a spatial and temporal composite analysis was developed, modeled after the analysis of the evolution of atmospheric heating associated with deep convection presented in Masunaga (2012). Here, CALIPSO dust layer observations were composited around both large- and small-scale convective events that were identified by the PATMOS-x convection algorithm to statistically quantify the influence of convective storm systems on the dust layer. Whenever convection was identified, the closest CALIPSO overpass to that location and time was used to supply corresponding aerosol information. Only coincident overpasses within ± 10 hr of the convection were considered, and the time differences were used to statistically track the influences of the convective storms through time. Vertical profiles of dust extinction from the two degree box surrounding each convective system were aggregated for each lead and lag interval between PATMOS-x convection and the CALIPSO aerosol observation. A schematic of this compositing technique is shown in Figure 6, which is adapted from Masunaga (2012). Because the analysis considers dust in the vicinity of convection, gaps where the lidar is fully attenuated by thick clouds are

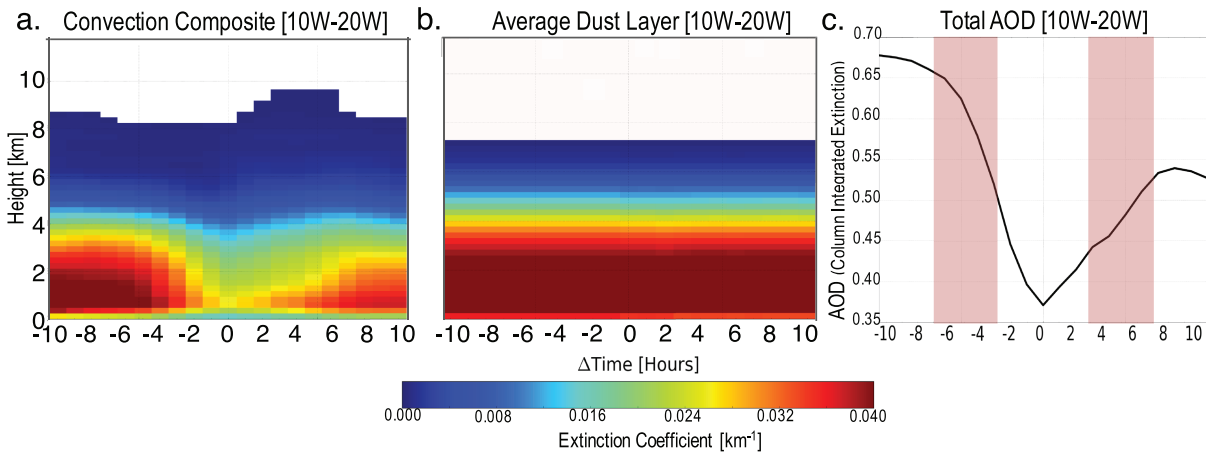


Figure 7. (a) Annual mean composite vertical distribution of height-resolved dust extinction coefficient as a function of time to the nearest convection from collocated Cloud Aerosol Lidar and Infrared Pathfinder Satellite Observations and Pathfinder Atmospheres Extended data for 10°W to 20°W. Statistics are shown for all the Cloud Aerosol Lidar and Infrared Pathfinder Satellite Observations profiles occurring 10 hr before and after identified convection. (b) Similar statistics obtained when all Pathfinder Atmospheres Extended pixels are included regardless of whether convection is present. (c) As in (a) but for column-integrated dust extinction coefficient. The red shaded regions are used to represent dust layer conditions before and after convection when representing wet deposition in section 5. Observations from 0°N to 35°N are included in the averages.

filled by interpolating CALIPSO observations from the nearest clear-sky regions on either side. To ensure that the PATMOS-x and CALIOP observations correspond to the same air mass, the CALIPSO ground track is advected with 500-millibar (mb) mean winds from Modern Era Retrospective Analysis for Research and Applications data to each PATMOS-x observation time and the presence of convection is determined from the PATMOS-x cloud products along this advected track.

This analysis was applied to 4 years of collocated CALIPSO and PATMOS-x observations from 2007 to 2010 to quantify how convection impacts the dust layer in each of seven, 10°, longitude bands across the tropical Atlantic Ocean from 10°W to 80°W. Using a 10° longitude resolution ensures that the dust layer remains within the band at all times analyzed before and after the overpass. Figure 7a shows the composite evolution of dust extinction over 20 hr around all incidences of convection identified with the PATMOS-x data set in the 10°W to 20°W longitude band. AOD_{dust} from the 2° box surrounding each convective pixel is averaged to represent the dust characteristics of the air mass in the vicinity of convection, since CALIPSO cannot directly observe dust in cloudy skies. Figure 7b illustrates the average dust layer between 10°W and 20°W independent of the presence of convection, while Figure 7c shows the total dust extinction for each time period around the passage of convection.

In the hours preceding identified convection along the CALIPSO track, the dust layer begins to decrease in thickness and dust extinction. This effect is evident as much as 3 to 5 hr before identified convection mostly likely due to the increased likelihood of precipitation in the vicinity of detected convective events along the CALIPSO track. When conditions are favorable for convection, convective plumes may be present in the domain that likely contribute to scavenging dust. At the time of convection, the dust layer thins dramatically and optical depths are reduced by up to 50% for as much as 5 hr after convection, indicative of enhanced deposition during the associated precipitation. The dust layer begins to recover around 7 to 9 hr after convection was initially identified as more dust is advected into the region but only returns to 60–70% of its preconvective characteristics. We gain a clear indication that these effects can be attributed to convection when these results are compared to Figure 7b. In the absence of identified convection, the average dust layer remains uniform across all time periods compared to the convective composite in Figure 7a. This life cycle is further illustrated in Figure 7c. Dust extinction rates are much larger and geometrically thicker in the hours leading up to the convective event, characteristic of the unperturbed SAL, while both depth and dust extinction are significantly decreased after the passage of convection. The effects of convection on dust concentration appear to be generally independent of the initial dust concentration as evidenced by the similar evolution observed further away from the source (Figure 8). In fact, all seven longitude bands (shown in Figures S1–S5 in supporting information) exhibit similar dust responses to the passage of convection.

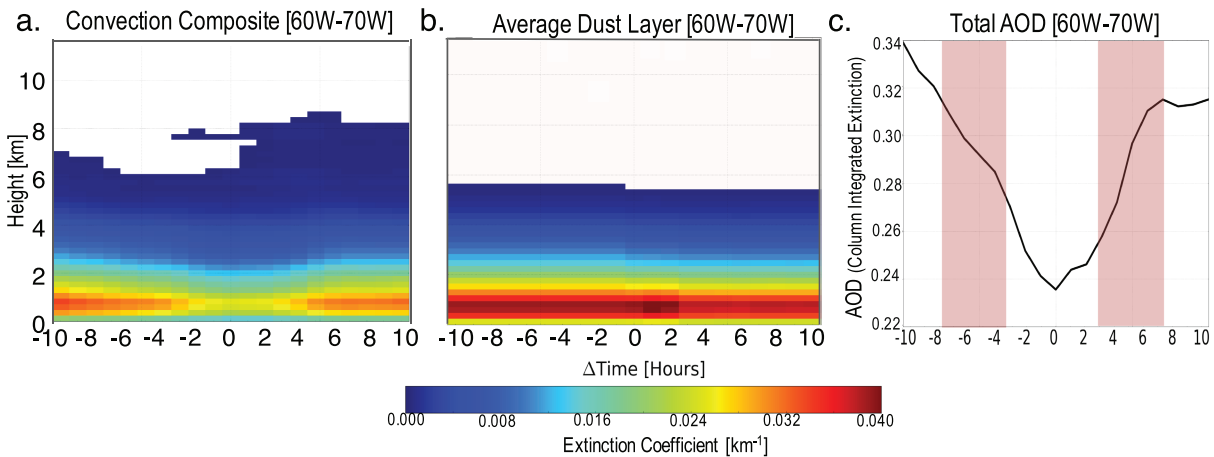


Figure 8. As in Figure 7 but for 60°W to 70°W.

However, the effect is most dramatic in regions closest to the source that have deeper initial dust layers in association with the SAL.

Interestingly, despite the significant overall depletion in AOD_{dust} owing to the passage of convection, Figures 7a and 8a both provide a visible indication of enhanced dust extinction aloft in the 6 hr following convection. The composite dust layer is observed to extend to about 2 km deeper, to 9.5 km between 10°W and 20°W and to 9 km between 60°W and 70°W in hours 1 through 6 after convection providing further evidence of dust lofting. To better quantify this effect, Figure 9a presents the average fraction of dust mass in the column that resides between 6 and 8, 8 and 10, and greater than 10 km associated with the passage of convection. Figure 9a indicates clear evidence of enhanced dust concentrations aloft following the passage of convection. Upper layers contribute proportionally more to the total column AOD after convection than before it. Thus, in addition to scavenging a significant fraction of the total dust from the column, the passage of convection leaves a more top-heavy dust profile in its wake. Such a signature does not exist when the data are not filtered for convection (Figure 9b). Lofting also occurs slightly before the time of convection, likely due to the turbulent environment associated with convection. Very few layers are observed at altitudes above 10 km (about 0.02%), even though these layers exist at levels similar to thunderstorm anvils in the tropics. These findings are consistent with Twohy et al. (2017) who demonstrated the existence of aerosol enhancement zones in aircraft measurements adjacent to anvil bases associated with Atlantic tropical cyclones, as well as with the numerical simulations of Herbener et al. (2016) who demonstrated similar peaks in upper level dust transport by tropical storms.

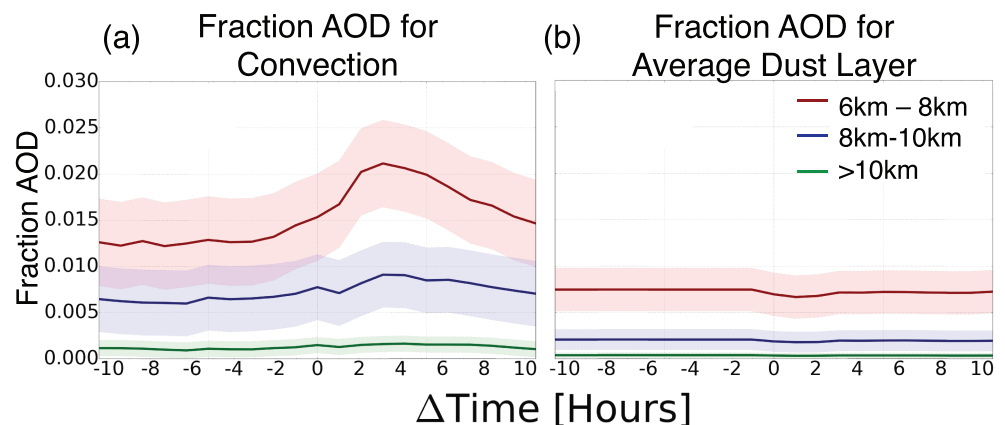


Figure 9. The fraction of column-integrated AOD_{dust} residing between 6–8, 8–10, and greater than 10 km as a function of time to identified convection (a) and in the absence of any convective screening (b). AOD = aerosol optical depth.

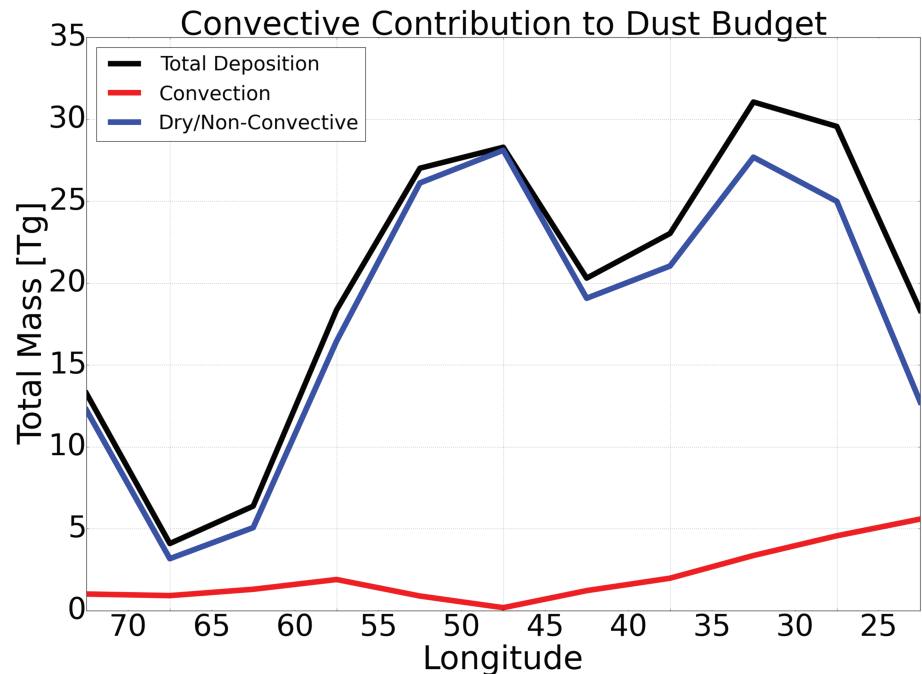


Figure 10. Total dust deposition budget (black line) for all longitude bands between 10°W and 80°W and the components owing to wet deposition by convection and dry/nonconvective deposition in the red and blue lines, respectively.

Comparing the effect of convection on lofted dust to the amount of dust at the same height levels in the average dust layer (Figure 9b) again provides strong evidence that convection enhances dust concentrations aloft. All dust mass and removal estimates are for the entire column and not explicitly the SAL. Besides a lack of any temporal variations in Figure 3b, the fraction of dust in the upper atmosphere is up to 3 times lower relative to unconditioned overall mean conditions compared to the times surrounding convective events. This increase in upper level dust concentrations when conditions are favorable for convection is consistent with the notion that convection is lofting dust aerosols into the atmosphere; however, the fraction of dust lofted by convection is fairly low (about 1.5%), relative to the amount scavenged by wet deposition (up to 15%). These results show that convection lofts dust aerosols to higher levels not only during individual organized storm events like those that were presented in SL17 but also during all convective events in this region.

5. An Attempt to Quantify Wet and Dry Deposition in the SAL Relative to Storm Passage

The preceding analysis provides a pathway for using observations to quantify the contribution of wet scavenging from convection to the net dust deposition from the SAL as it crosses the Atlantic Ocean. To contrast the amount of dust removed by wet and dry deposition, Figure 10 shows the integrated effects of convective events on the dust budget across the tropical Atlantic Ocean and computes the corresponding contribution from “dry deposition” as a residual. Dry deposition in this instance also includes wet scavenging from nonconvective precipitation events that do not meet our PATMOS-x screening criteria. The black line in Figure 10 represents the total amount of deposition derived from Figure 2, while the red and blue lines indicate the amount of dust removed through wet and dry deposition, respectively. A total of 6.44 Tg or 28% of all dust was removed from the atmosphere during identified convective periods in the 10–20°W longitude band, and a total of 0.92 Tg or 8% was removed in the 60–70°W band. Across the entire tropical Atlantic, convection removes 17.45 Tg of dust accounting for 15% of the total deposition between 10°W and 80°W.

The vertical redistribution of dust mass by convection can be estimated by subtracting the fraction of total dust mass at each altitude prior to and after convection. The time periods are defined here in Figure 7: 3 to 7 hr before convection and 3 to 7 hr after convection. This time window was chosen because it represents mean conditions before and after convection. The full composites in Figures 7a and 8a demonstrate the

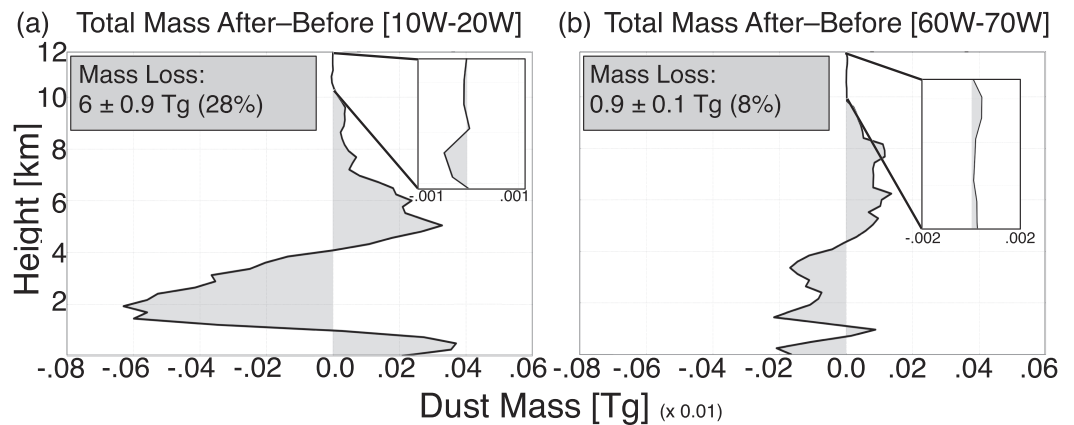


Figure 11. Vertical redistribution of dust by convection for the (a) 10–20°W and (b) 60–70°W longitude bands. Positive values represent layers where the fraction of dust mass is increased by the storm passage, while negative values correspond to reduced dust mass fraction after storm passage.

complete evolution of the dust layer at all hours before and after convection and suggest that the impacts of convection are primarily realized within 6 hr after which the dust layer begins a slow recovery to its pre-convection levels. Additional time windows were examined, (e.g., 2–6, 3–6, and 4–8 hr), but we found no significant changes to the net deposition amounts over all longitude bands (<2% difference). Figure 11a presents the resulting vertical redistribution of dust mass for the 10–20°W convective composite, while Figure 11b represents the 60–70°W longitude band. Positive values represent layers where the dust fraction is increased by convection, while negative values portray layers where convection reduces dust concentration.

Consistent with Figure 10, a significant amount of dust is removed between the surface and 4 km in both longitude bands, indicative of the removal of the SAL after convective events. There is a low-level enhancement of dust after convection in the 10–20°W band that may be caused by evaporating raindrops below cloud base, returning dust aerosol to the atmosphere as opposed to scavenging it back to the ocean. Similar to Figure 7 of Twohy et al. (2017) and Figure 8 of van den Heever et al. (2017), dust mass increases in layers between 6 and 12 km after convection is identified, highlighting the important role convection plays in lofting dust aerosols into the upper troposphere. Approximately 1.61% of dust was found to be lofted above 6 km in the 10–20°W longitude band and 1.71% in the 60–70°W longitude band. On average $1.5\% \pm 0.6\%$ is lofted above 6 km in all seven longitude bands. Although the results for only two longitude bands are presented in detail, all seven bands exhibit similar results with dust lofted to layers between 6 and 12 km at the expense of the SAL between the surface and 4 km after convection.

6. Discussion and Conclusions

This work examines the evolution of CALIPSO dust aerosol profiles in the context of high time resolution geostationary cold cloud information to assess the role of convection in redistributing mineral dust in the atmosphere. Collocated A-Train aerosol data and time resolved estimates of convection from PATMOS-x were utilized to gain insights into the time evolution of aerosol field in response to the passage of convection. Using a novel compositing technique to track changes in AOD throughout a convective storm life cycle, dust budgets were analyzed to quantify the fraction of dust that is removed in the atmosphere through wet deposition processes and the fraction that is transported to the upper troposphere by convective storm systems.

On average, 160 ± 24 Tg of dust leave the west coast of Africa. As the dust layer advects westward across the Atlantic, 1.83 Tg of dust are removed per 100 km, and wet deposition by convection accounts for $15\% \pm 7\%$ of this deposition. Further analysis of the evolution of the vertical dust distribution reveals a small but measurable number of dust layers at upper levels in the atmosphere between 6 and 12 km that appear to be linked to convection. Lofted dust layers are not only apparent closest to the dust source but are also prevalent further across the Atlantic Ocean, accounting for 1.61% of dust between 10°W and 20°W and 1.71% of dust between 60°W and 70°W. A composite analysis of the evolution of the dust layer during the passage of

convection suggests that convection is the primary mechanism for the presence of these layers. On average, convection lofts $1.5\% \pm 0.6\%$ of dust aerosol to altitudes greater than 6 km.

The upper level dust fractions and deposition of dust particles postconvection shown here complement cloud-resolving model studies that show both fractional amounts of lofted dust to the upper troposphere and dry deposition of dust after convection (Herbener et al., 2016) and in situ observations of enhanced dust concentrations around tropical storm anvils at similar heights (Twohy et al., 2017). Quantifying the downstream effects of these phenomena on climate requires further investigation. Establishing the dependence on storm size, structure, and intensity, for example, would provide valuable insight in how convective storms transform the dust layer, influencing the Earth's radiation budget and impacting ice cloud microphysical properties.

Acknowledgments

The CALIPSO aerosol data used in this study are provided by the NASA Langley Research Center's (LaRC) ASDC DAAC and are managed by the NASA Earth Science Data and Information System (ESDIS) project. The PATMOS-x data were obtained through the University of Wisconsin Space Science and Engineering Center's data center. Direct access to this data is available via ftp from the ftp.ssec.wisc.edu/pub/patmosx/data/hdf/level2b website. This work was supported by the National Science Foundation and Technology Center under projects AGS-1409359, AGS-1409686, and AGS-1408028. We are grateful for the reviewers' comments.

References

- Arkin, P. A. (1979). The relationship between fractional coverage of high cloud and rainfall accumulations during GATE over the B-scale array. *Monthly Weather Review*, *107*(10), 1382–1387.
- Arkin, P., & Meisner, B. (1987). The relationship between large-scale convective rainfall and cold cloud over the Western Hemisphere during 1982–84. *Monthly Weather Review*, *115*(1), 51–74.
- Bouniol, D., Roca, R., Fiolleau, T., & Poan, D. E. (2016). Macrophysical, microphysical, and radiative properties of tropical mesoscale convective systems over their life cycle. *Journal of Climate*, *29*(9), 3353–3371.
- Braun, S. A. (2010). Reevaluating the role of the Saharan air layer in Atlantic tropical cyclogenesis and evolution. *Monthly Weather Review*, *138*(6), 2007–2037.
- Brindley, H. E., & Russell, J. E. (2009). An assessment of saharan dust loading and the corresponding cloud-free longwave direct radiative effect from geostationary satellite observations. *Journal of Geophysical Research*, *114*, D23201. <https://doi.org/10.1029/2008JD011635>
- Bullard, J. E., Baddock, M., Bradwell, T., Crusius, J., Darlington, E., Gaiero, D., et al. (2016). High-latitude dust in the Earth system. *Reviews of Geophysics*, *54*, 447–485. <https://doi.org/10.1002/2016RG000518>
- Carlson, T. N., & Prospero, J. M. (1972). The large-scale movement of Saharan air outbreaks over the northern equatorial Atlantic. *Journal of Applied Meteorology*, *11*(2), 283–297.
- Chen, G., Ziemba, L., Chu, D., Thornhill, K., Schuster, G., Winstead, E., et al. (2011). Observations of Saharan dust microphysical and optical properties from the Eastern Atlantic during NAMMA airborne field campaign. *Atmospheric Chemistry and Physics*, *11*(2), 723–740.
- Deng, M., Mace, G. G., Wang, Z., & Okamoto, H. (2010). Tropical Composition, Cloud and Climate Coupling Experiment validation for cirrus cloud profiling retrieval using CloudSat radar and CALIPSO lidar. *Journal of Geophysical Research*, *115*, D00J15. <https://doi.org/10.1029/2009JD013104>
- Duce, R. A. (1986). The impact of atmospheric nitrogen, phosphorus, and iron species on marine biological productivity, *The role of air-sea exchange in geochemical cycling* (pp. 497–529). Dordrecht: Springer.
- Dulac, F., Tanré, D., Bergametti, G., Buat-Ménard, P., Desbois, M., & Sutton, D. (1992). Assessment of the African airborne dust mass over the western Mediterranean Sea using Meteosat data. *Journal of Geophysical Research*, *97*(D2), 2489–2506.
- Dunion, J. P., & Velden, C. S. (2004). The impact of the Saharan air layer on Atlantic tropical cyclone activity. *Bulletin of the American Meteorological Society*, *85*(3), 353–365.
- Evan, A. T., Dunion, J., Foley, J. A., Heidinger, A. K., & Velden, C. S. (2006). New evidence for a relationship between Atlantic tropical cyclone activity and African dust outbreaks. *Geophysical Research Letters*, *33*, L19813. <https://doi.org/10.1029/2006GL026408>
- Fu, R., Del Genio, A. D., & Rossow, W. B. (1990). Behavior of deep convective clouds in the tropical Pacific deduced from ISCCP radiances. *Journal of climate*, *3*(10), 1129–1152.
- Fung, I. Y., Meyn, S. K., Tegen, I., Doney, S. C., John, J. G., & Bishop, J. K. (2000). Iron supply and demand in the upper ocean. *Global Biogeochemical Cycles*, *14*(1), 281–295.
- Goudie, A., & Middleton, N. (2001). Saharan dust storms: Nature and consequences. *Earth-Science Reviews*, *56*(1), 179–204.
- Grousset, F. E., Ginoux, P., Bory, A., & Biscaye, P. E. (2003). Case study of a chinese dust plume reaching the french alps. *Geophysical Research Letters*, *30*(6), 1277. <https://doi.org/10.1029/2002GL016833>
- Ham, S.-H., Kato, S., Rose, F. G., Winker, D., L'Ecuyer, T., Mace, G. G., et al. (2017). Cloud occurrences and cloud radiative effects (CRES) from ceres-calipso-cloudsat-MODIS (CCC) and cloudsat radar-lidar (RL) products. *Journal of Geophysical Research: Atmospheres*, *122*, 8852–8884. <https://doi.org/10.1002/2017jd026725>
- Haynes, J. M., L'Ecuyer, T. S., Stephens, G. L., Miller, S. D., Mitrescu, C., Wood, N. B., & Tanelli, S. (2009). Rainfall retrieval over the ocean with spaceborne W-band radar. *Journal of Geophysical Research*, *114*, D00A22. <https://doi.org/10.1029/2008JD009973>
- Haynes, J., L'Ecuyer, T., Vane, D., Stephens, G., & Reinke, D. (2014). Level 2-C precipitation column algorithm product process description and interface control document.
- Haywood, J., Francis, P., Osborne, S., Glew, M., Loeb, N., Highwood, E., et al. (2003). Radiative properties and direct radiative effect of Saharan dust measured by the C-130 aircraft during SHADE: 1. Solar spectrum. *Journal of Geophysical Research*, *108*(D18), 8577. <https://doi.org/10.1029/2002JD002687>
- Heidinger, A. K., Evan, A. T., Foster, M. J., & Walther, A. (2012). A naive Bayesian cloud-detection scheme derived from CALIPSO and applied within PATMOS-x. *Journal of Applied Meteorology and Climatology*, *51*(6), 1129–1144.
- Heidinger, A. K., Foster, M. J., Walther, A., & Zhao, X. (2014). The pathfinder atmospheres-extended AVHRR climate dataset. *Bulletin of the American Meteorological Society*, *95*(6), 909–922.
- Henderson, D. S., L'Ecuyer, T., Stephens, G., Partain, P., & Sekiguchi, M. (2013). A multisensor perspective on the radiative impacts of clouds and aerosols. *Journal of Applied Meteorology and Climatology*, *52*(4), 853–871.
- Herbener, S. R., Saleeby, S. M., Heever, S. C., & Twohy, C. H. (2016). Tropical storm redistribution of Saharan dust to the upper troposphere and ocean surface. *Geophysical Research Letters*, *43*, 10,463–10,471. <https://doi.org/10.1002/2016GL070262>
- Herbener, S. R., Van Den Heever, S. C., Carrió, G. G., Saleeby, S. M., & Cotton, W. R. (2014). Aerosol indirect effects on idealized tropical cyclone dynamics. *Journal of the Atmospheric Sciences*, *71*(6), 2040–2055.
- Houze, R. A. (2004). Mesoscale convective systems. *Reviews of Geophysics*, *42*, RG4003. <https://doi.org/10.1029/2004RG000150>

- Houze, R. A. Jr. (2014). *Cloud dynamics* (Vol. 104). Oxford, UK: Academic Press, Elsevier.
- Huneeus, N., Schulz, M., Balkanski, Y., Griesfeller, J., Prospero, M., Kinne, S., et al. (2011). Global dust model intercomparison in AeroCom phase I. *Atmospheric Chemistry and Physics*, *11*, 7781–7816.
- Husar, R. B., Prospero, J. M., & Stowe, L. L. (1997). Characterization of tropospheric aerosols over the oceans with the NOAA advanced very high resolution radiometer optical thickness operational product. *Journal of Geophysical Research*, *102*(D14), 16,889–16,909.
- Igel, M. R., Drager, A. J., & Heever, S. C. (2014). A cloudsat cloud object partitioning technique and assessment and integration of deep convective anvil sensitivities to sea surface temperature. *Journal of Geophysical Research: Atmospheres*, *119*, 10,515–10,535. <https://doi.org/10.1002/2014JD021717>
- Im, E., Wu, C., & Durden, S. L. (2005). Cloud profiling radar for the CloudSat mission. In *Radar conference, 2005 IEEE International* (pp. 483–486) IEEE.
- Karyampudi, V. M., & Pierce, H. F. (2002). Synoptic-scale influence of the Saharan air layer on tropical cyclogenesis over the eastern Atlantic. *Monthly Weather Review*, *130*(12), 3100–3128.
- Kaufman, Y., Koren, I., Remer, L., Tanré, D., Ginoux, P., & Fan, S. (2005). Dust transport and deposition observed from the Terra-Moderate Resolution Imaging Spectroradiometer (MODIS) spacecraft over the Atlantic Ocean. *Journal of Geophysical Research*, *110*, D10S12. <https://doi.org/10.1029/2003JD004436>
- Koren, I., Kaufman, Y. J., Washington, R., Todd, M. C., Rudich, Y., Martins, J. V., & Rosenfeld, D. (2006). The Bodélé depression: A single spot in the Sahara that provides most of the mineral dust to the Amazon forest. *Environmental Research Letters*, *1*(1), 014005.
- L'Ecuyer, T. S., & Jiang, J. H. (2010). Touring the atmosphere aboard the A-Train. *Physics Today*, *63*(7), 36–41.
- Lebsock, M. D., L'Ecuyer, T. S., & Stephens, G. L. (2011). Detecting the ratio of rain and cloud water in low-latitude shallow marine clouds. *Journal of Applied Meteorology and Climatology*, *50*(2), 419–432.
- Liu, G., Curry, J. A., & Sheu, R.-S. (1995). Classification of clouds over the western equatorial Pacific Ocean using combined infrared and microwave satellite data. *Journal of Geophysical Research*, *100*(D7), 13,811–13,826.
- Liu, Z., Vaughan, M., Winker, D., Kittaka, C., Getzewich, B., Kuehn, R., et al. (2009). The CALIPSO lidar cloud and aerosol discrimination: Version 2 algorithm and initial assessment of performance. *Journal of Atmospheric and Oceanic Technology*, *26*(7), 1198–1213.
- Liu, D., Wang, Z., Liu, Z., Winker, D., & Trepte, C. (2008). A height resolved global view of dust aerosols from the first year CALIPSO lidar measurements. *Journal of Geophysical Research*, *113*, D16214. <https://doi.org/10.1029/2007JD009776>
- Liu, D., Wang, Y., Wang, Z., & Zhou, J. (2012). The three-dimensional structure of transatlantic African dust transport: A new perspective from CALIPSO LIDAR measurements. *Advances in Meteorology*, *2012*, 850704.
- Maddox, R. A. (1980). Mesoscale convective complexes. *Bulletin of the American Meteorological Society*, *61*, 1374.
- Mahowald, N. M., Kloster, S., Engelstaedter, S., Moore, J. K., Mukhopadhyay, S., McConnell, J. R., et al. (2010). Observed 20th century desert dust variability: Impact on climate and biogeochemistry. *Atmospheric Chemistry and Physics*, *10*(22), 10875–10893.
- Mapes, B. E., & Houze, R. A. Jr. (1993). Cloud clusters and superclusters over the oceanic warm pool. *Monthly Weather Review*, *121*(5), 1398–1416.
- Maring, H., Savoie, D., Izaguirre, M., Custals, L., & Reid, J. (2003). Mineral dust aerosol size distribution change during atmospheric transport. *Journal of Geophysical Research*, *108*(D19), 8592. <https://doi.org/10.1029/2002JD002536>
- Masunaga, H. (2012). A satellite study of the atmospheric forcing and response to moist convection over tropical and subtropical oceans. *Journal of the Atmospheric Sciences*, *69*(1), 150–167.
- Min, Q.-L., Li, R., Lin, B., Joseph, E., Wang, S., Hu, Y., et al. (2009). Evidence of mineral dust altering cloud microphysics and precipitation. *Atmospheric Chemistry and Physics*, *9*(9), 3223–3231.
- Moulin, C., Lambert, C., Dayan, U., Masson, V., Ramonet, M., Bousquet, P., et al. (1998). Satellite climatology of african dust transport in the Mediterranean atmosphere. *Journal of Geophysical Research*, *103*(D11), 13,137–13,144.
- Myhre, G., Grini, A., Haywood, J. M., Stordal, F., Chatenet, B., Tanré, D., et al. (2003). Modeling the radiative impact of mineral dust during the saharan dust experiment (SHADE) campaign. *Journal of Geophysical Research*, *108*(D18), 8579. <https://doi.org/10.1029/2002JD002566>
- Omar, A. H., Winker, D. M., Vaughan, M. A., Hu, Y., Trepte, C. R., Ferrare, R. A., et al. (2009). The CALIPSO automated aerosol classification and lidar ratio selection algorithm. *Journal of Atmospheric and Oceanic Technology*, *26*(10), 1994–2014.
- Pavlonis, M. J., Heidinger, A. K., & Uttal, T. (2005). Daytime global cloud typing from AVHRR and VIIRS: Algorithm description, validation, and comparisons. *Journal of Applied Meteorology*, *44*(6), 804–826.
- Pratt, A. S., & Evans, J. L. (2009). Potential impacts of the Saharan air layer on numerical model forecasts of North Atlantic tropical cyclogenesis. *Weather and Forecasting*, *24*(2), 420–435.
- Prospero, J. (1996). Saharan dust transport over the North Atlantic Ocean and Mediterranean: An overview, *The impact of desert dust across the Mediterranean* (pp. 133–151). Dordrecht: Springer.
- Reiff, J., Forbes, G. S., Spiekma, F. T. M., & Reynolds, J. (1986). African dust reaching northwestern Europe: A case study to verify trajectory calculations. *Journal of Climate and Applied Meteorology*, *25*(11), 1543–1567.
- Rosenfeld, D., Clavner, M., & Nirel, R. (2011). Pollution and dust aerosols modulating tropical cyclones intensities. *Atmospheric Research*, *102*(1-2), 66–76.
- Ryder, C., Highwood, E., Lai, T., Sodemann, H., & Marsham, J. (2013). Impact of atmospheric transport on the evolution of microphysical and optical properties of Saharan dust. *Geophysical Research Letters*, *40*, 2433–2438. <https://doi.org/10.1002/grl.50482>
- Sassen, K., DeMott, P. J., Prospero, J. M., & Poellot, M. R. (2003). Saharan dust storms and indirect aerosol effects on clouds: Crystal-face results. *Geophysical Research Letters*, *30*(12), 1633. <https://doi.org/10.1029/2003GL017371>
- Sauter, K. E., & L'Ecuyer, T. S. (2017). Observational evidence for the vertical redistribution and scavenging of Saharan dust by tropical cyclones. *Geophysical Research Letters*, *16*, 1456–1475. <https://doi.org/10.1002/2017GL074166>
- Schmetz, J., Pili, P., Tjemkes, S., Just, D., Kerkmann, J., Rota, S., & Ratier, A. (2002). An introduction to Meteosat second generation (MSG). *Bulletin of the American Meteorological Society*, *83*(7), 977–992.
- Stephens, G. L., Vane, D. G., Boain, R. J., Mace, G. G., Sassen, K., Wang, Z., et al. CloudSat Science Team (2002). The CloudSat mission and the A-Train: A new dimension of space-based observations of clouds and precipitation. *Bulletin of the American Meteorological Society*, *83*(12), 1771–1790.
- Storer, R., Heever, S., & L'Ecuyer, T. (2014). Observations of aerosol-induced convective invigoration in the tropical east Atlantic. *Journal of Geophysical Research: Atmospheres*, *119*, 3963–3975. <https://doi.org/10.1002/2013JD020272>
- Sun, B., Free, M., Yoo, H. L., Foster, M. J., Heidinger, A., & Karlsson, K.-G. (2015). Variability and trends in US cloud cover: ISCCP, PATMOS-x, and CLARA-A1 compared to homogeneity-adjusted weather observations. *Journal of Climate*, *28*(11), 4373–4389.
- Tegen, I., & Fung, I. (1995). Contribution to the atmospheric mineral aerosol load from land surface modification. *Journal of Geophysical Research*, *100*(D9), 18707–18726.

- Tegen, I., Lacis, A. A., & Fung, I. (1996). The influence on climate forcing of mineral aerosols from disturbed soils. *Nature*, *380*(6573), 419.
- Tobin, I., Bony, S., & Roca, R. (2012). Observational evidence for relationships between the degree of aggregation of deep convection, water vapor, surface fluxes, and radiation. *Journal of Climate*, *25*(20), 6885–6904.
- Twohy, C., Anderson, B., Ferrare, R., Sauter, K., L'Ecuyer, T., van den Heever, S., et al. (2017). Saharan dust, tropical convection and aerosol enhancement zones. *Journal of Geophysical Research: Atmospheres*, *122*, 8833–8851. <https://doi.org/10.1002/2017JD026933>
- Van den Heever, S. C., Carrió, G. G., Cotton, W. R., DeMott, P. J., & Prenni, A. J. (2006). Impacts of nucleating aerosol on florida storms. Part I: Mesoscale simulations. *Journal of the Atmospheric Sciences*, *63*(7), 1752–1775.
- van den Heever, S., Herbener, S., Sauter, K., Twohy, C., Saleeby, S., L'Ecuyer, T., & Ekman, A. (2017). The transport and processing of dust by tropical cyclones.
- Walther, A., & Heidinger, A. K. (2012). Implementation of the daytime cloud optical and microphysical properties algorithm (DCOMP) in PATMOS-x. *Journal of Applied Meteorology and Climatology*, *51*(7), 1371–1390.
- Weinzierl, B., Petzold, A., Esselborn, M., Wirth, M., Rasp, K., Kandler, K., et al. (2009). Airborne measurements of dust layer properties, particle size distribution and mixing state of Saharan dust during SAMUM 2006. *Tellus B*, *61*(1), 96–117.
- Winker, D. M., Pelon, J. R., & McCormick, M. P. (2003). The CALIPSO mission: Spaceborne lidar for observation of aerosols and clouds, *Third international Asia-Pacific environmental remote sensing remote sensing of the atmosphere, ocean, environment, and space* pp. 1–11): International Society for Optics and Photonics.
- Winker, D. M., Vaughan, M. A., Omar, A., Hu, Y., Powell, K. A., Liu, Z., et al. (2009). Overview of the CALIPSO mission and CALIOP data processing algorithms. *Journal of Atmospheric and Oceanic Technology*, *26*(11), 2310–2323.
- Young, S. A., Vaughan, M. A., Kuehn, R. E., & Winker, D. M. (2013). The retrieval of profiles of particulate extinction from Cloud-Aerosol Lidar and Infrared Pathfinder Satellite Observations (CALIPSO) data: Uncertainty and error sensitivity analyses. *Journal of Atmospheric and Oceanic Technology*, *30*(3), 395–428.
- Yu, H., Chin, M., Bian, H., Yuan, T., Prospero, J. M., Omar, A. H., et al. (2015). Quantification of trans-Atlantic dust transport from seven-year (2007–2013) record of CALIPSO lidar measurements. *Remote Sensing of Environment*, *159*, 232–249.
- Yu, H., Chin, M., Winker, D. M., Omar, A. H., Liu, Z., Kittaka, C., & Diehl, T. (2010). Global view of aerosol vertical distributions from CALIPSO lidar measurements and GOCART simulations: Regional and seasonal variations. *Journal of Geophysical Research*, *115*, D00H30. <https://doi.org/10.1029/2009JD013364>
- Yuan, J., Houze, R. A. Jr., & Heymsfield, A. J. (2011). Vertical structures of anvil clouds of tropical mesoscale convective systems observed by CloudSat. *Journal of the Atmospheric Sciences*, *68*(8), 1653–1674.
- Zhu, X., Prospero, J., & Millero, F. (1997). Diel variability of soluble Fe (II) and soluble total Fe in North African dust in the trade winds at Barbados. *Journal of Geophysical Research*, *102*(D17), 21297–21305.
- Zipser, E. J., Twohy, C., Tsay, S.-C., Thornhill, KLee, Tanelli, S., Ross, R., et al. (2009). The Saharan air layer and the fate of African easterly waves: NASA's AMMA field study of tropical cyclogenesis. *Bulletin of the American Meteorological Society*, *90*, 1137.